Research Square

Preprints are preliminary reports that have not undergone peer review.
They should not be considered conclusive, used to inform clinical practice,
or referenced by the media as validated information.

# Sediment bypassing limits future subdelta growth in backstepping Lower Mississippi River Delta, Louisiana, USA

**Faith Walton**

fwalto1@lsu.edu

Louisiana State University

**Samuel Bentley**

Louisiana State University

**Yanda Ou**

Louisiana State University

**Z. George Xue**

Louisiana State University

**Giancarlo Portocarrero Cortez**

Louisiana State University

**Emily Wei**

Louisiana State University

**Muhamad Farid Geonova**

Louisiana State University

**Mead Allison**

Tulane University

**Ziyan Lei**

Louisiana State University

**Nathan Figueredo**

Louisiana State University

**Alba Romero-Martin**

Universidad de Cádiz

**Jameson Woodall**

Louisiana State University

**D'Metrie King**

Louisiana State University

**Article**

**Keywords:**

**Posted Date:** September 10th, 2026

**DOI:** https://doi.org/10.21203/rs.3.rs-10756764/v1

**License:** This work is licensed under a Creative Commons Attribution 4.0 International License.
Read Full License

**Additional Declarations:** No competing interests reported.

# Abstract

Anthropogenic activities have driven the Mississippi River Delta (MRD) to retrograde above and below sea level, a fate shared by many large coastal river deltas. However, the role of seasonal sediment dispersal to the coastal ocean in shaping the delta remains unclear. Here we present oceanic dispersal and seabed deposition patterns and quantity for the river's total fine-grained sediment load. Using $^{7}$Be as a seasonal tracer of fluvial sedimentation, we share a mass-balance sediment budget for ~ 3000 km$^{2}$ of the subaqueous MRD for the year 2025. Findings show that $^{7}$Be sediment deposition rates (SDR) depend on oceanographic conditions and seabed morphology as well as sediment supply. A bypass zone exists on the northeast shelf despite the local opening of multiple large passes and hydrologic backstepping of the river. Additionally, SDR patterns indicate that fine-grained sediment from these passes is advected southwestward towards Pass a Loutre and South Pass where it is deposited, highlighting oceanic dispersal processes in overall delta evolution. While $^{7}$Be SDRs show sediment deposition across the delta front, plume sedimentation alone is not enough to continue delta front progradation. Findings will be used to improve predictions of the evolution of the MRD and aid future management.


# 1. Introduction

Globally, coastal river deltas have developed over the last several millennia through a balance of sediment supply, sediment retention, relative sea-level change, and organic contributions [1]. Many river basins worldwide have experienced drastic reductions in sediment load since the start of widespread dam building and channel engineering in the late 19th and mid-20th centuries [2]. Natural and anthropogenic subsidence contribute to accelerating relative sea-level rise for many deltas [3] [4] [5]. Together, reduced basin sediment supply and increasing relative sea-level rise are destabilizing the pre-Anthropocene sediment balance [2], causing many deltas to subside, erode, and shrink [6]. Those that are not losing land have experienced an increase in sediment supply due to human-driven sediment erosion, mostly associated with deforestation [7].

Subaqueous portions of deltas are extensive, provide the foundations for subaerial deltaic growth, and are subject to the same sediment balance as regions at sea level [8]. Sediment dispersal to subaqueous deltas is controlled through fluvial discharge interacting with oceanographic processes and (in some cases) gravity-driven processes [6]. Defining sediment dispersal processes and pathways within the subaqueous delta provides insights into the dynamics that shape delta morphology and contribute to the sustainability of the delta complex [9] [10].

The role of sediment mass balance in sustaining subaqueous deltas has recently received increased research attention due to global challenges facing deltas, but it remains poorly understood for the Mississippi River Delta (MRD), the largest delta in North America. The MRD presently hosts the primary navigation outlet (Southwest Pass), numerous communities, and important industry and ecosystems[11]. From the river during an annual flood event and its shelf, recent research shows that discharge and

seabed patterns are changing rapidly for the lowermost ~ 100 km of the Birdsfoot of the MRD, which now appears to be in the early stages of backstepping [12] [13]. This region of the river contains at least 12 distributary outlets, up from four a century ago. Over the last ~ 20 years, discharge of water and sediment has shifted rapidly towards upstream outlets and away from the historically dominant southernmost outlets [13] [14] (Southwest Pass, South Pass, and Pass a Loutre; Fig. 1). Offshore of these southern outlets, subaqueous clinothems have been prograding for centuries but have now stalled growth and have locally begun to retreat [15]. These changes are accelerating processes that have been documented since at least 1960 [16]. For example, the Neptune Pass outlet (~ 70 km upstream from the Southwest Pass entrance) evolved from a small canal prior to 2016 [16] to a substantial distributary capturing at least 16% of the Mississippi River's flow by 2025 [16]. A new subdelta lobe had begun to form in the receiving basin adjacent to Neptune Pass by 2025, when a rock barrier was installed to limit flow through the pass [17].

To predict the future of this rapidly evolving delta, a more detailed understanding of the offshore sediment mass-balance is needed. The goal of this study is to track the mass balance of seasonal sediment discharge along with offshore dispersal and deposition to gain insight into the ongoing evolution of the most recent lobe of the MRD, the Balize or Birdsfoot Delta and its sustainability. One of our ultimate goals in the present MissDelta effort [18] is to develop a full seasonal and decadal mass balance of sediment transported by the river and deposited in the river channel, adjacent wetlands, and coastal ocean seabed [19]. In the present study, we present the first steps to achieve this by quantifying offshore seasonal fine-grained sediment deposition on the Birdsfoot subaqueous delta to provide insights into modern sediment dispersal patterns and aid in constructing numerical models of deltaic sedimentation and morphodynamics. This study focuses on tracing the seasonal plume and related fine-grained sediment deposition across the entire Birdsfoot subaqueous delta region in water depths > 1m during the 2025 peak discharge period of the Mississippi River. Sediment %<62.5 μm accounts for approximately 90% of the river's total load [14]. Simulations from a high-resolution regional ocean model were used to explore the role of oceanographic processes in sediment dispersal. Constraining the other budget components above is ongoing at longer timescales, this study focuses on a seasonal sedimentation budget as a first step towards examining subaqueous sediment retention.[20] [21] [22] [23] [24] [25]. Based on observations above, we trial two hypotheses in the present manuscript, that (1) oceanic sediment-dispersal pathways are highly dependent on water depth, hydrodynamics, and oceanographic conditions, and (2) that sediment load advected seaward through outlets upstream of Head of Passes (HOP) while increasing, is not deposited proximally to outlets, but is advected more distally in the subaqueous delta.

# 2. Methodology

# 2.1 Study Site

The study area encompasses ~ 3000 $km^2$ of seabed of the subaqueous Mississippi River Delta (MRD) from West Bay to offshore of Neptune Pass (Fig. 1). Core sites are located 1.4–42.5 km offshore and in water depths ranging from 1.9 to 444 meters below sea level (mbsl). The Mississippi River (MR) drainage basin feeding our study area encompasses an area of 3.4 x $10^6$ $km^2$, making it the largest riverine system in North America [10]. Over the past ~ 100 years, the MR has experienced an approximate 50% decline in sediment load because of anthropogenic modifications [27].

# 2.2 Fieldwork and Core Sampling/Processing

Field work was performed from March to June 2025. Multicores (MC) (Ocean Instruments MC 800, 10 cm diameter, 60 cm penetration) were collected across most of the study area from the *R/V Point Sur* in early May 2025. In early June 2025, pushcores (PsC) (7.5 cm diameter, 40 cm penetration) were collected from a small boat in water too shallow for the larger ship. Sampling locations were determined using: (1) a square grid with a boundary guided by Earth Scan Laboratory MODIS historical satellite imagery of the river plume [28]; and (2) multi-beam bathymetry and sub-bottom seismic data [29] [30]. Multicores were collected 6–10 days after peak river discharge (Fig. 2), and pushcore collection occurred 29–30 days after peak river discharge. On the *R/V Point Sur*, cores were subsampled at 3 cm intervals and packed into sample bags for analysis. Pushcores were recovered, capped with overlying water, and kept upright until subsampling at 3 cm intervals in the lab at Louisiana State University. Wet samples were weighed, then dried for > 24 h at 60 ℃ and reweighed to determine water content, then ground into a powder using a mortar and pestle. An average of 35 g of powdered sediment was then sealed into a plastic screw-top canister 7.5 cm in diameter and 3 cm thick and held for $^7$Be analysis, described below.

# 2.3 Grain Size

Grain size analysis was conducted using a Beckman Coulter LS 13 320 Laser Diffraction Particle Size Analyzer. Wet samples of ~ 1 $cm^3$ were processed with hydrogen peroxide to oxidize organics, then added to a 0.05% solution of sodium metaphosphate to prevent flocculation and run through the analyzer.

# 2.4 Radionuclide Analysis

This study uses the radionuclide $^7$Be (natural cosmogenic, $t_{1/2}$ = 53.3 days, 477 keV gamma peak) to calculate local sediment deposition rates (SDR, g $cm^{-2}$ $d^{-1}$) which are then spatially interpolated (see below). Cosmogenic $^7$Be is produced in the atmosphere, delivered to Earth's surface by wet deposition and then adsorbed onto sediments [31]. It is used as a tracer of short-term riverine sediment deposition due to its short half-life and particle reactivity that leads to concentration in fluvial sediments at higher activities than found in open-marine settings [31] [32] hence forming a tracer of sediments recently derived from fluvial sources.

A conventional approach to calculating SDRs from $^{7}$Be sediment-activity profiles involves the use of a log-linear regression of activity versus depth. This approach requires that $^{7}$Be activity decreases with increasing sediment depth, which is not always the case [33]. A different approach is used here based on the sediment inventory of a particle-bound radioisotope (decays per minute per cm$^{2}$ (dpm cm$^{-2}$)), the flux required to maintain that inventory over several half-lives of that radioisotope [31] (dpm cm$^{-2}$ y$^{-1}$), and the radioisotope activity of sediment delivered to the seabed (dpm g$^{-1}$). Sediment-bound inventories for $^{7}$Be were calculated using Equation A [34].

$$I = \Sigma\, p_s \Delta\, z(1 - \Phi_n) A_n \quad \text{Eq. A}$$

Where I is inventory (dpm cm$^{-2}$), $\rho_s$ is mineral density (g cm$^{-3}$), $\Delta z$ is the thickness of sample (3 cm), $\Phi_n$ is porosity at depth *n* calculated by water loss at 60°C, and $A_n$ is activity (dpm g$^{-1}$).

The radioisotope flux J (dpm cm$^{-2}$ y$^{-1}$) required to maintain this inventory over several half-lives of that isotope is [34]:

$J = \lambda I$ Eq. B

where λ is the decay constant of the radioisotope (t$^{-1}$). The SDR of radioisotope-laden sediment required to produce the inventory can be estimated by of the activity of sediment depositing on the seabed ($A_i$, dpm g$^{-1}$) is known:

$$SDR = I\lambda\, A_i^{-1} \quad \text{Eq. C}$$

This approach assumes the system is near steady state, in which radioisotope deposition has occurred over timescales comparable to 4–5 half-lives of the radioisotope. This assumption is addressed in the Discussion.

Previous studies in the region have identified separate fluvial and vertical atmospheric-fallout sources [35] [36]. Here, because $^{7}$Be activities mostly reach non-detectable levels at the edges of our study area, we focus on the predominance of fluvial supply only, and the SDR necessary to sustain the observed inventory. The value of $A_i$ was estimated by averaging values of $^{7}$Be measured in sediment samples from three sources: suspended sediment in the Mississippi River channel in Baton Rouge (see Supplementary Methodology- *Radionuclide Analysis* for sampling methods), Louisiana USA 228 km above HoP (Fig. 2), suspended sediment in the oceanic plume ~ 5 km offshore of the Mississippi River mouth, and the average of all sediment-surface activities measured in the 0–3 sample of each core with detectable $^{7}$Be (see Supplementary Methodology-*Radionuclide Analysis* for more information on determining detection limits). Uncertainty for this rate (± 91%) was estimated using the square root of the sum of squares approach, incorporating 25% uncertainty for $^{7}$Be inventories (from average detector uncertainty per sample), 58% standard deviation for all Ai measurements, and 51% uncertainty in the time over which sediment was delivered to the seabed before sampling.

## 2.5 Interpolation Methods

To determine the sediment deposition rates for the study area, we created an interpolated surface of $^{7}$Be SDRs measured from individual core locations. The spatially integrated sediment mass deposition rate was calculated with the Surface Volume tool [37] and converted to $10^{6}$ metric tons $d^{-1}$.

The interpolated surface of $^{7}$Be SDRs measured from individual core locations projected in UTM was created using the Delaunay triangulation method in ArcPro GIS software, and the resulting TIN surface was linearly transformed into a raster surface [38]. This methodology was used to adhere to trends in the data and minimize extrapolated surface curvature, rather than to create a surface with the smooth appearance of a natural distribution. Abrupt transitions result from triangulation over abrupt local gradients in data distribution (e.g., in East Bay, where $^{7}$Be sedimentation rates vary widely over a small region). The resulting surface was clipped to connect 1-km buffers inshore and offshore of sample locations.

## 2.6 Calculating Apparent Mass Deposition

Apparent Mass Deposition (AMD) for each region and the entire study area was calculated using the spatially integrated sediment mass deposition rates calculated as described in the previous section, the total fines load measured at the Belle Chasse station calculated back one year from the date of the last seabed core sample, and three estimated durations of peak sediment delivery to the seabed.

Suspended sediment load delivered to the study area by the Mississippi River was calculated utilizing monthly measurements at the USGS Mississippi River station at Belle Chasse, LA (USGS-07374525) to construct a sediment ratings curve. This location (River Mile 73; RK117) is located immediately upriver of the first unmanaged exit (e,g., Mardi Gras Pass) into the study area. Because $^{7}$Be is adsorbed only onto fines, measurements at Belle Chasse for total load were adjusted for measured %<62.5 μm fraction to define a fines only measured load [39] [40] [41]. Quadratic best fit regression curves were used to calculate daily sediment load constructed using only fines measurements for WY2025 (See Supplementary Fig. S1, Supplementary Methodology *Sediment Load Calculations* Eq. 1–2); these proved similar to a three-year data compilation (WY2023-2025) of measurements. Daily average water discharge from the USGS Belle Chasse station gage was applied to the fines sediment ratings curve equation to derive the final daily loads calculation in tons/d. The total loads utilized are the sum of the daily load of fines during the period up to one calendar year prior to the last date of sample collection (06/18/2024-06/19/2025).

For each region of interest, the spatially integrated mass deposition rates were multiplied by the duration of peak sediment delivery to determine Apparent Mass Deposition. The duration of three time periods of fines sediment delivery to the seabed were summed over 213 days (4-times the half-life of $^{7}$Be, over which our typical samples decay below detection), 154 days (estimated duration of peak sediment load from USGS station USGS-07374000 in Baton Rouge), and 103 days (period spanning the first river

sampling to final seabed sampling).The AMD was then divided by the total fines sediment load calculated from the Belle Chasse values and multiplied by 100 to determine the percent of the total sediment load captured by that region.

# 2.7 Bed Shear Stress Estimation

We extracted the bed shear stress from a regional ocean model setup to evaluate the hydrodynamics that affect sediment dispersal and deposition. The model was built on the Coupled Ocean–Atmosphere–Wave–Sediment Transport (COAWST) modeling system [42] (version 3.8), where the ocean model ROMS is online coupled with SWAN through the Model Coupling Toolkit2 (MCT). ROMS is a three-dimensional, free-surface, terrain-following ocean model that solves the Reynolds-averaged Navier–Stokes equations under hydrostatic and Boussinesq assumptions using a split-explicit time-stepping scheme [43] [44] [45]. SWAN solves the wave action balance equation in Eulerian form and represents wave propagation over varying bathymetry and currents, together with key source and sink processes such as wind input, wave–wave interactions, whitecapping, bottom friction, and depth-induced breaking [46].

For ROMS, the southern and eastern open boundaries were forced with daily sea level, three-dimensional and depth-integrated currents, salinity, and temperature from the Hybrid Coordinate Ocean Model (HYCOM) Global Ocean Forecasting System 3.1 ((https://www.hycom.org/dataserver/gofs-3pt1/analysis, last access on March 12, 2026) which includes data assimilation through the Navy Coupled Ocean Data Assimilation system [47] [48] [49] [50]. Boundary conditions used Chapman radiation for free surface[48], Flather radiation for depth-integrated momentum [51], a gradient condition for turbulent kinetic energy, and mixed radiation–nudging for three-dimensional momentum, temperature, and salinity, with nudging timescales of 1 day for inflow and 30 days for outflow [52]. Initial ocean conditions were taken from the same HYCOM product. Atmospheric forcing fields, including 10 m winds, radiation fluxes, precipitation, 2 m air temperature, sea level pressure, and 2 m relative humidity, were obtained from the National Centers for Environmental Prediction (NCEP) Climate Forecast System Reanalysis Version 2 (CFSv2) 6-hourly products at ~ 22 km resolution [50]. River input was represented by 63 rivers, divided into 404 point sources that supplied time-varying freshwater, temperature, and horizontal momentum based on discharge, using daily observations from US Geological Survey National Water Information System, and Mexico National Water Commission (for rivers in Mexico's territory). More detailed description of the hydrodynamic setups in ROMS are given in Ou and Xue (2024) [53] supported by the Pacific Islands Ocean Observing System. SWAN was initialized from a calm ocean state. We output six-hourly three-dimensional and depth-integrated current velocity, water level, three-dimensional temperature and salinity, significant wave height, mean wave direction at the surface, peak wave period at the surface, bottom current-induced shear stress, bottom wave-induced shear stress, and the maximum bottom shear stress induced by the combined effects of currents and waves at the cruise observation sites.

The coupled system was configured on an Arakawa C-grid at ~ 1 km horizontal resolution over the Gulf of America (previously referred to as the Gulf of Mexico), with 1709 × 1799 interiorpoints and 18 sigma

layers in ROMS. A wetting–drying scheme [54] was included to better resolve shallow coastal regions. The ROMS baroclinic time step was 90 s with 40 barotropic substeps, while the SWAN computational time step was 300 s. ROMS exchanged information with SWAN every 90 s, and SWAN returned updates every 300 s through MCT.

The model's performance of hydrodynamics and sediment transport has been validated through a 20-year hindcast covering the period of 1993 to 2012 [55]. For this study, we extended the model simulation to the end of year 2025 and refined the resolution of Zang et al.'s (2019) model from 5 km to 1 km. While the model does provide sediment deposition outputs, this model's resolution of 1 km is not at the resolution needed to compare directly against the observational data. While COAWST also has a mature sediment transport module that can represent sediment dynamics on both event and decadal scales [55] [56], for this study, we focused mainly on combined wave-current bed shear stress to explain observed sediment deposition patterns. In the coupled ROMS–SWAN–sediment system, bottom shear stress for suspended sediment resuspension is calculated using a wave–current bottom boundary layer (BBL) formulation [57]. ROMS provides the near-bottom current velocity, while SWAN provides wave parameters such as wave height, period, direction, and bottom orbital velocity. The BBL model combines the current-induced stress with wave-enhanced stress to estimate the near-bed skin-friction shear stress. Sediment is resuspended when this skin-friction stress exceeds the critical shear stress for erosion [58], after which suspended sediment is transported in the water column by advection, diffusion, and settling processes. A 400m higher-resolution model with full sediment-transport parameters and more detailed river-ocean coupling is under development for implementation in the near future [21].

## 3 Results

# 3.6 Sediment Properties and Measured Initial $^{7}$Be Activity

Sediments in the top-most ~ 10 cm of all cores are light brown muds with high water content (porosities 70–90%) and mean grain sizes of 0.14-0.0013 mm (fine sand-clay). Activities of $^{7}$Be used for $A_i$ in Equation C are shown in Fig. 2, averaging 5.7 ± 4.4 dpm $g^{-1}$. The highest activity of suspended sediment is in the river plume offshore of SW Pass (9.9 dpm $g^{-1}$). The lowest value (2.1 dpm $g^{-1}$) is the average of all core-surface (0–3 cm) samples (Fig. 1). Activities of suspended sediment samples collected in Baton Rouge near river km 367 above Head of Passes are intermediate (4.6–6.1 dpm $g^{-1}$).

# 3.7 Calculated and Interpolated SDR and AMD

Figure 3 shows a geospatial representation of SDR (Eq. C) at each discrete core site overlain on an interpolated SDR surface. Values of SDR and inventory are shown in Supplementary Tables S1-3. Along the outer perimeter of the shaded polygon in Fig. 3, $^{7}$Be activities and inventory are only above the detection limit northeast of Neptune Pass and west of Southwest Pass, indicating that we were likely able to capture the full extent of plume deposition along the majority of our study area's perimeter.

SDRs are highest offshore of South Pass and remain elevated in shallow water in regions between certain passes in the eastern half of the study area (Baptiste-Collette to Main Pass, Main Pass to Pass a Loutre, Pass a Loutre to East Bay) and generally diminish in seaward directions. Some locations in shallow water (namely off Baptiste Collette and Main Pass at stations 110, 15, and 95, Fig. 3) that show high SDRs are associated with cores collected from bathymetric lows that are only evident in local navigation charts and are not resolved in regional bathymetric data used for model simulations due to the coarse horizontal resolution of bathymetry grids (see below). Offshore and northwest of Neptune Pass, $^{7}$Be is not detectable in our data.

Integrating SDRs for the entire polygon in Fig. 3 provides an overall SDR estimate of $0.17 \pm 0.15 \times 10^{6}$ t $d^{-1}$ for the study area (Table 1). Subdividing this into three subregions yields (Fig. 3, Table 1) $0.52 \times 10^{6}$ t $d^{-1}$ for the northeastern subregion, $0.74 \times 10^{6}$ t $d^{-1}$ for the southeastern subregion, and $0.42 \times 10^{6}$ t $d^{-1}$ for the western region, around Southwest Pass, which is the primary Mississippi River navigation channel, and presently has the highest discharge of the three major historical outlets of the Birdsfoot terminus.

Table 1

Table 1
Comparison of the calculated sediment loads for the Birdsfoot Delta to offshore SDR estimated using $^{7}Be$.

| **Sediment Discharge ($10^6$ t $y^{-1}$) WY2025** | **Possible Durations of peak sediment load** | **Data source for duration** | **Daily offshore SDR from $^{7}Be$ analysis ($10^6$ t $d^{-1}$) overall and for subregions (Fig. 2)** | **Apparent Mass Deposition for different durations (days) of daily SDR ($10^6$ t)** | **Percent of annual discharge** |
|---|---|---|---|---|---|
| 48.7 | 213 d | 4 half-life limit of method | 0.17 (Total) | **213 d** | 74% (Total) |
| | | | .052 (NE, 31%) | 36 (Total) | 22% (NE) |
| | | | .074 (SE, 44%) | 11 (NE) | 32% (SE) |
| | | | .042 (W, 25%) | 16 (SE) | 18% (W) |
| | | | | 9 (W) | |
| | 154 d | USGS sediment flux data for station USGS-07374000 | | **154 d** | 54% (Total) |
| | | | | 26 (Total) | 16% (NE) |
| | | | | 8 (NE) | 23% (SE) |
| | | | | 11 (SE) | 13% (W) |
| | | | | 6 (W) | |
| | 103 d | Days between first river sampling and final ocean coring | | **103 d** | 36% (Total) |
| | | | | 17 (Total) | 11% (NE) |
| | | | | 5 (NE) | 16% (SE) |
| | | | | 8 (SE) | 9% (W) |
| | | | | 4 (W) | |

# 3.3 Modeled Bed Shear Stress

Spatially interpolated results (Fig. 4) and time-series point measurements (Supplementary Fig. S2) show resuspension thresholds of 0.1 Pa for freshly deposited Mississippi River plume mud and coarse silt grains and 0.6 Pa [59] [60] [61] for more consolidated plume mud and coarse sand grains. In shallow water stations (0–20 m water depth), bed shear stresses are persistently higher for the modelled period than those in deep water stations (40–444 m water depth). Peaks in bed shear stress throughout the modelled period are associated with cold front events (Supp. Figure 1).

Regional wave, current, and combined bed shear stress distributions from model results are shown for two periods: one period of low combined bed shear stresses (06/30/2025, Fig. 4a), and period of near-

peak bed shear stresses (04/05/2025, Fig. 4b). The resuspension thresholds defined above allow us to delineate regions of low, moderate, and high shear stress at different times and locations. Although continental shelf bathymetry is complex in the study area, approximate depths of these resuspension thresholds for periods of high energy are 7–45 mbsl (0.1–0.6 Pa); and low energy periods are 2–7 mbsl (0.1–0.6 Pa).

During high energy periods, current bed shear stress fields indicate that sediment is being reworked offshore. Wave-induced bed shear stress fields indicate that waves are interacting heavily with the seafloor offshore of SEP, SP, EB, PaL and where the water begins to shallow into Breton Sound offshore of the Main Pass area. Low energy periods see similar patterns in how waves interact with the seafloor, but at a lower magnitude, while the current-induced bed shear stress fields show a direction change in the Breton Sound (NW to SE) and East Bay (W to E) regions.

During the near-peak period, nearly all the delta front region (south of SP, SWP, and PAL) has elevated bed shear stresses > 0.6 Pa (Fig. 4b). During these energetic times, only the distal portions of the delta front (depths > 20 mbsl) have bed shear stresses < 0.1 Pa. In contrast, during the low-energy period, only selected portions of the delta front have bed shear stresses > 0.1 Pa, and no parts > 0.6 Pa. Another area with elevated shear stress is offshore of the eastern Birdsfoot, where bed shear stresses exceed 0.6 Pa during peak energy and 0.1 Pa during low-energy periods. The shear stress contours in Breton Sound follow the arc of the Chandeleur Islands. Finally, southwest portions of the Birdsfoot Delta have highly heterogeneous patterns in bed shear stress.

## 4 Discussion

# 4.1 Constraining Initial $^{7}$Be Activity

Because the actual value of $A_i$ from Eq. c is not known, SDR calculations use an average of all $A_i$ values shown in Fig. 2, yielding 5.7 dpm $g^{-1}$. Measured $A_i$ values (Eq. C) vary greatly across environments, likely due to a combination of variations in grain size distribution of sediment in suspension and seabed mixtures of older and younger sediments for the 0-3cm samples [39] [62]. For example, sand grains were observed in river samples and would likely dilute $^{7}$Be activities, whereas the oceanic plume sample appeared to be mainly silts and clays, effectively concentrating the $^{7}$Be activity for that sample.

## *4.2 Determining the Offshore Fine-Grained Sediment Budget*

To develop a mass balance of river supply and offshore deposition, the fluvial sediment load must be defined. The most recent measurements of suspended fine-grained sediment load reaching the Birdsfoot Delta outlets were calculated from the Belle Chasse monitoring station totaling 48.7 Mt $yr^{-1}$. To compare our sediment budget results from our SDR-interpolated surface to the total annual sediment load of the MR, we calculated Apparent Mass Deposition (AMD) for the entire study area and the three regions we defined (Table 1). For a duration of 213 d, the AMD is 36 × $10^{6}$ t, which is equivalent to ~ 74%

of the annual suspended fines load at Belle Chasse. For a duration of 154 d, the AMD is 26 × $10^6$ t, equivalent to ~ 53% of annual suspended load. For a duration of 103 d, the AMD is 17 × $10^6$ t, equivalent to ~ 36% of the annual suspended load at Belle Chasse. Of regions defined in Fig. 3 and Table 1, the SE polygon captures the most sediment, accounting for 16–32% of the annual suspended load.

## 4.3 Sediment transport pathways

Offshore sediment deposition patterns appear to contrast with water discharge patterns from outlets above and below Head of Passes reported by Allison et al. 2023 for 2004–2022 (yellow arrows in Fig. 3). For example, discharge from Neptune Pass and nearby Fort St Phillip and Ostrica passes climbed from 14% in 2004 to 31% of total upstream flow in 2022. However, our data following peak 2025 discharge show little detectable $^7$Be in the northern part of the NE polygon offshore of these passes (Fig. 3). In Spring 2025, the US Army Corps of Engineers (USACE) reported that Neptune Pass captured 16% of total Mississippi flow, introducing the threat of accelerated river capture and threats to navigation [13]. In Summer 2025, after our sampling collection had been completed, USACE placed boulders in the Neptune Pass channel to restrict flow to ~ 6% [17]. This change to channel discharge is likely to impact future inshore and offshore sedimentation patterns.

More 2025 sediment deposition from the spring sediment plume is evident offshore of Baptiste Collette and Main Pass, which represented 14% of total river water discharge in 2022 [13] (declining from 20% in 2004; Fig. 3). The largest AMD rate appears to occur in the SE polygon, from Pass a Loutre to South Pass and East Bay (Table 1, Fig. 3), which in 2022 discharged only 2% of Mississippi River total flow [13], with total discharge below Head of Passes declining from 54% in 2004 to 42% in 2022 [13]. We know of no processes that could alter suspended sediment concentrations substantially among these two passes and infer that sediment loads have probably tracked water discharge rates over this period. Collectively, these patterns suggest that oceanographic processes are transporting sediments southward along the eastern margin of the Birdsfoot, and river-discharge patterns play a lesser role in proximal offshore deposition patterns for the NE polygon and offshore of PaL. Other factors, such as maintenance dredging within channels done by an ACE Hopper Dredge within Southwest Pass could be impacting sediment delivery offshore of SWP, the primary navigation channel. PaL and SP are not regularly dredged by the ACE.

To test whether oceanographic currents exert more controls on $^7$Be AMD than fluvial inputs, we compared our SDR-interpolated surface to model-simulated combined current- and wave-driven bed shear stresses in the region (Fig. 4). Areas < 0.1 Pa are defined hydrodynamically as depositional zones. For areas that exceed 0.6 Pa, we consider them to be “bypass” zones, where combined bed shear stresses are too high for fine-grained sediment to settle out of suspension. Areas that fall in between those contours are transitional areas that act as temporary storage for deposited sediments that may then be resuspended during higher-energy events and worked elsewhere. Figure 4 shows the regional bed shear stresses for a “low-energy" and “high-energy” period and how these contours compare with our SDR interpolated surface.

We further explore the possible impact of wave-current resuspension by examining two contrasting regions: shallow water and deeper water. An example of a shallow water (above fair-weather wave base (FWWB)) site is offshore of Neptune Pass, 47PsC, in ~3m water depth with high fluvial water and sediment discharge. An example of a deeper water (20–50 m depth, from between FWWB and storm wave base (SWB) to below SWB) site is offshore of PaL, 99MC, in ~ 44m water depth with low fluvial water and sediment discharge. During low-energy conditions (Fig. 4c), both locations have bed-shear stresses < 0.1 Pa, and so are potentially depositional. During high-energy conditions (Fig. 4d), bed shear stresses offshore of Neptune Pass are > 0.1 Pa, conditions that could resuspend recently deposited plume sediments or sediments that have been in deposition longer and are more consolidated. The deep-water location off PaL is < 0.1Pa during the high-energy period and shows that deposition is occurring despite low discharge through the pass. This suggests that oceanographic conditions are bringing in sediment to be deposited. In contrast, seabed conditions in waters offshore of South Pass, namely at 63MC, ~ 21m, are at or below 0.1 Pa, and so are more likely depositional during low energy periods. During high energy periods, site 63MC is within the transitional zone of 0.1–0.6 Pa creating the potential for sediment resuspension. This site is likely still influenced by both fluvial input and oceanographic currents driving sediment E-W across the delta front. We can see the impact of oceanographic currents on plume sedimentation in satellite imagery, further supporting the importance of oceanographic processes (Supplementary Fig. S3).

While maps of low- and high-energy periods can reveal spatial variability, time-series measurements can help us determine the potential for sediment deposition/resuspension in different water depths (Supplementary Fig. S2). Stations at depths < 10 mbsl are consistently above the 0.1 Pa bed shear stress threshold for deposition of sediments throughout time. This indicates that sediment leaving the river in those areas (East Bay/South Pass, Baptiste Collette) can likely remain in suspension and be transported elsewhere. In some other shallow-water regions of the Louisiana coast where suspended sediment concentrations are high, such as the Chenier Plain [63] in SW Louisiana or on the Amazon shelf [64], formation of fluid muds due to high suspended sediment concentrations attenuate wave-energy and promote sediment deposition in open shallow-water settings. The core data and results of this study do not support the existence of this phenomenon in our study area. Grain size distributions and lack of $^{7}$Be signatures within the 0-3cm sediment samples in this region, chiefly at stations offshore of NP, are not indicative of fluid muds (Supplementary Tables 1–3).

The time series for stations at 10–40 mbsl reveals that bed shear stresses can dip below the 0.1Pa threshold for deposition. This indicates that there is potential for episodic deposition and resuspension. These areas can be considered areas for temporary sediment storage, including local bathymetric lows offshore of Baptiste Collette and Main Pass (Fig. 3). Once such bathymetric lows are infilled, higher bed shear stresses on the now-shallower seabed may evolve into sediment bypass areas like the other shallow-water regions. Stations offshore Baptiste Collette and Main Pass (110MC, 15MC, 95MC) with high SDRs sit in this category.

Together, SDR patterns and bed shear stress time series indicate that the shallow, friction-dominated western region of Breton Sound that Neptune Pass, Main Pass and other upstream passes empty into is a bypass region, which was created by the previous infilling of accommodation by the St. Bernard lobe of the MR [29] [65], leading to elevated bed shear stresses. Based on observations and interpretations above, we propose that sediments are being reworked from the shallow waters off Neptune Pass and offshore Breton Sound where sediment input has increased in recent years and are being deposited in deeper waters offshore in depocenters that span Pass a Loutre to South Pass.

Stations in water depths > 40 m do have periods during the time series where they exceed bed shear stresses > 0.1 Pa required for resuspension of sediments but are more often below that 0.1Pa threshold, allowing for more deposition of fine-grained sediments either from river plumes or wave-current processes. We attribute higher SDR percentages of the SE region (10–20%) to these conditions. Thus, on seasonal time scales, peak sediment deposition from the settling of river plume sediment occurs in water depths > 40m where bed shear stresses are low.

To summarize, substantial sources of sediment discharge from the river to the coastal ocean have shifted upstream from historically important outlets at the Birdsfoot terminus over the last 20 to 60 years [13] [14] [15]. Sandy distributary-mouth bars are forming within several km of channel mouths [16]. However, despite uncertainties in our seasonal sedimentation estimates, fine-grained sediment deposition offshore of these outlets (Fig. 3) does not appear to be accumulating at rates sufficient to create muddy subaqueous deltas comparable to those formed in the 19th century and earlier at Baptiste Collette, Main Pass (Cubit's Gap), and below Head of Passes. Those muddy subaqueous clinothems formed the foundation for much of the modern Birdsfoot Delta and infilled the limited accommodation that had been largely filled by the relict St. Bernard Delta [29] [64\3]. Instead, large amounts of fine-grained sediment are bypassing shallow waters and being deposited distally from the outlets with the largest sediment discharges, and in locations where extensive accommodation will likely prevent the formation of emergent subdeltas. One prominent example from this category includes the station (63 MC, 21 mbsl) offshore South Pass, which has the highest SDR values in the whole region even though flow through SP is low [13]. Despite increased seasonal sediment load to offshore sediment depocenters, however, this increased sediment flux to areas > 40 mbsl is not enough to slow down the retrogradation of the subaqueous delta [15] [22]. Seasonal plume sedimentation along the MRDF is also not enough to explain long-term sedimentation patterns, as important drivers of sedimentation along the MRDF include gravity-driven flows and sediment delivery through extensive gully systems in the region [25] [66] [67].

Heavy modifications to the MRD system introduce further complications into a system that has already been strained by subsidence and natural bypass. Coastal deltas worldwide [68] [69] [70] are experiencing decreasing sediment and water loads [2]. Increasing rates of sea level rise and decreasing sediment output to coastal areas have caused major deltas to enter a stage of retrogradation. Sustained decreases in sediment load suggest that many deltas will continue to struggle to maintain both subaerial and subaqueous stability and continue to experience land loss. Hydrologic backstepping of rivers, as

seen in the Mississippi River, may not necessarily lead to the formation of new subdelta lobes or reactivation of older subdelta lobes upstream, as accommodation may not be sufficient for deposition if the basins have previously been infilled. Thus, coastal managers cannot assume that sediment lost from upstream outlets will stay within the system. An ultimate goal of the MissDelta effort is to use this budget, which will be wrapped into a system-wide budget, to help improve long-term geomorphic models for delta evolution [18] [19]. The work outlined in this paper is not only informative for the MRD system alone, but also for struggling deltas worldwide.

## Conclusions

This study of seasonal offshore sediment deposition using $^{7}$Be is an initial step to create a mass-balance sediment budget for the Birdsfoot Delta of the Mississippi River Delta and contributes to our understanding of future delta evolution. The sediment load that reaches Head of Passes is historically decreasing and the delta has begun backstepping, making this study a significant resource for understanding how delta morphology is changing under seasonal conditions. The major conclusions of this study are:

1. $^{7}$Be analysis shows that significant sediment deposition occurs near major outlets in deeper water, but not near major outlets in shallow water, despite the largest sediment loads likely being discharged in shallow-water, upstream locations.
2. Oceanographic conditions, namely wave conditions, do not allow for deposition of fine-grained, muddy sediments flowing through outlets that empty into in the shallow Breton Sound basin. Sediments likely stay in suspension or are reworked, resuspended, and moved into deeper water.
3. This has formed a depocenter offshore of the Pass a Loutre and South Pass outlets that have historically decreasing sediment and water loads. Despite increased sediment deposition rates from suspension, this is not enough to offset subaqueous delta retrogradation.
4. Under present conditions, it is unlikely that there will be a period of renewed growth of thick, muddy subaqueous clinoforms in response to increased upstream discharge in shallow water areas off passes like Neptune Pass and Baptiste Collette. This area of the inner shelf consists of friction-dominated, shallow receiving basins with little remaining accommodation; localized bathymetric lows exist where aggradation of muds does occur but is depth-limited.
5. Subaqueous delta growth in shallow water (Neptune Pass) is restricted to the sandy portion of the Mississippi River's suspended sediment load, which is ~ 10% of the river's total load.
6. Seasonal suspended sediment deposition in deeper water is a contributor to deposition of a thin prodelta in water > 40 mbsl on the Mississippi River Delta Front but is only one of the main factors in long-term sedimentation rates and patterns, which also includes sediment transport through gullies by gravity-driven flows.

Globally, human modifications to river delta hydrology modify the dispersal of spring flood sediment to subaqueous deltas. While this study found that geology, wave-climate, currents, and sediment grain size all interplay to dictate how plume sediment is dispersed, it also demonstrates the outsize effects of

anthropogenic changes to seasonal sediment dispersal. Therefore, this work establishes a baseline of sediment dispersal during peak river discharge, which is the first step in understanding delta sustainability. Similar work in delta complexes worldwide will guide efforts to manage deltas effectively.

## Declarations

# Additional Information

**Competing Interests Statement:**

The authors declare no conflicts of interest.

**Funding**

This study was supported by the Military Logistics Independent Research Project in 2023.

**Disclosure**

The authors declared no potential conflicts of interest with respect to the research, authorship, and/or publication of this article.

**Availability of Data**

The data supporting the findings of this study are available from the corresponding author upon reasonable request.

**Declaration of Generative AI and AI-Assisted Technologies in the Writing Process**

During the preparation of this work, AI-assisted technology was used solely for language translation and polishing of the manuscript. The authors reviewed and edited the content as needed and take full responsibility for the content of the publication.

**Conflict of interest statement**

The authors declared no potential conflicts of interest with respect to the research, authorship, and/or publication of this article.

## References

1. Paola, C. & Martin, J. M. Mass-balance effects in depositional systems. *J. Sediment. Res.* **82**, 435–450. https://doi.org/10.2110/jsr.2012.38 (2012).
2. Syvitski, J. P. M. Deltas at risk. *Sustain. Sci.* **3**, 23–32. https://doi.org/10.1007/s11625-008-0043-3 (2008).

3. Ericson, J. P., Vorosmarty, C. J., Dingman, S. L., Ward, L. G. & Meybeck, M. Effective sea-level rise and deltas: causes of change and human dimension implications. *Glob Planet. Chang.* **50**, 63–82. https://doi.org/10.1016/j.gloplacha.2005.07.004 (2006).
4. Syvitski, J. P. M. et al. Sinking deltas due to human activities. *Nat. Geosci.* **2**, 681–686. https://doi.org/10.1038/ngeo629 (2009).
5. Nicholls, R. J. et al. A global analysis of subsidence, relative sea-level change and coastal flood exposure. *Nat. Clim. Change*. **11**, 338–342. https://doi.org/10.1038/s41558-021-00993-z (2021).
6. Syvitski, J. et al. Large deltas, small deltas: Toward a more rigorous understanding of coastal marine deltas. *Glob Planet. Change*. **218** https://doi.org/10.1016/j.gloplacha.2022.103958 (2022).
7. Global-scale human impact on delta morphology has. led to net land area gain https://doi.org/10.1038/s41586-019-1905-9
8. Slingerland, R. et al. Anatomy and growth of a Holocene clinothem in the Gulf of Papua. *J. Geophys. Res.* **113** https://doi.org/10.1029/2006JF000628 (2008).
9. Wright, L. D. & Nittrouer, C. A. Dispersal of river sediments in coastal seas: Six contrasting cases. *Estuaries Coasts*. **18**, 494–508. https://doi.org/10.2307/1352367 (1995).
10. Walsh, J. P. & Nittrouer, C. A. Fine-grained sediment dispersal on continental margins. *Mar. Geol.* **263**, 34–45. https://doi.org/10.1016/j.margeo.2009.03.016 (2009).
11. Cornwall, W. A river with a mind of its own. *Science* **387**, 130. https://doi.org/10.1126/science.adv7636 (2025).
12. Bentley, S. J. et al. Mississippi River source-to-sink system. *Earth-Sci. Rev.* **153**, 139–174. https://doi.org/10.1016/j.earscirev.2015.11.001 (2016).
13. Allison, M. A. et al. Water loss impacts on Mississippi River channel sustainability. *Hydrol. Process.* **37** https://doi.org/10.1002/hyp.15004 (2023).
14. Allison, M. A. et al. Water and sediment budget for the lower Mississippi–Atchafalaya River. *J. Hydrol.* **422–423**, 84–97. https://doi.org/10.1016/j.jhydrol.2012.02.020 (2012).
15. Maloney, J. M. et al. Mississippi River subaqueous delta retrogradation. *Mar. Geol.* **400**, 12–23. https://doi.org/10.1016/j.margeo.2018.03.001 (2018).
16. Kolker, A. S. et al. Distributary development in a 21st century river: The evolution of Neptune Pass and its delta, the largest new offshoot of the Mississippi River. *PLoS ONE*. 20. https://doi.org/10.1371/journal.pone.0320502 (2025).
17. U.S. Army Corps of Engineers. *Environmental Assess. #589: Neptune Pass. Rock. Closure* (2022).
18. MissDelta Initiative. https://missdelta.org/.
19. Allison, M. A. & Bentley, S. J. February. Introducing the Mississippi River Delta Transition Initiative (MissDelta). *AGU Ocean Sciences Meeting* (2024).
20. Wilson, C. et al. Seasonal organic and inorganic deposition in the Balize Delta marshes. *GCAGS/GCSSEPM Convention* (2026).

21. Du, R. et al. Plume sedimentation on the Mississippi River Delta Front: A preliminary modeling study. *GCAGS/GCSSEPM Convention* (2026).
22. Walton, F. et al. Spring flood dispersal offshore of the Mississippi River Delta. *AGU Annual Meeting* (2025).
23. Woodall, J. et al. Sediment transport and accumulation in the Anthropocene offshore of Pass a Loutre, Mississippi River Delta, USA. *AGU Annual Meeting* (2025).
24. Brannum, S. et al. Discharge and suspended sediment concentration variations across subdeltas in the lower Mississippi River Delta highlight areas of land loss. *AGU Annual Meeting* (2025).
25. Portocarrero, G. et al. Assessing a sediment budget for an interdistributary bay in the Mississippi River Delta: East Bay, Louisiana. *AGU Annual Meeting* (2025).
26. Earth Resources Observation and Science (EROS) Center. Coastal National Elevation Database (CoNED) Project - Topobathymetric Digital Elevation Model (TBDEM) [Dataset]. U.S. Geological Survey, (2017). https://doi.org/10.5066/F7Z60MHJ
27. Coleman, J. M. & Gagliano, S. M. Cyclic sedimentation in the Mississippi deltaic plain. *Gulf Coast Assoc. Geol. Soc. Trans.* **14**, 67–80 (1964).
28. Earth Scan Laboratory. MODIS Louisiana Coast Truecolor. (2026).
29. Wei, E. et al. Sediment bypass offshore Eastern Birdsfoot Delta. *Mar. Geol.* 107814, (2026). https://doi.org/10.1016/j.margeo.2026.107814
30. Baldwin, W. E., Ackerman, S., Worley, C. R., Danforth, W. W. & Chaytor, J. High-resolution geophysical data collected along the Mississippi River Delta front offshore of southeastern Louisiana, U.S. Geological Survey Field Activity 2017-003-FA [Dataset]. United States Geological Survey – Woods Hole Coastal and Marine Science Center. https://doi.org/10.5066/F7X929K6 (2018).
31. Taylor, A. et al. Assumptions and challenges in the use of fallout beryllium-7 as a soil and sediment tracer in river basins. *Earth-Sci. Rev.* **126**, 85. https://doi.org/10.1016/j.earscirev.2013.08.002 (2013).
32. Galler, J. J. & Allison, M. A. Estuarine controls on fine-grained sediment storage in the Lower Mississippi and Atchafalaya Rivers. *Geol. Soc. Am. Bull.* **120**, 386–398. https://doi.org/10.1130/B26060.1 (2008).
33. Sommerfield, C. K. et al. 7Be as a tracer of flood sedimentation on the northern California continental margin. *Cont. Shelf Res.* **19**, 335–361. https://doi.org/10.1016/S0278-4343(98)00090-9 (1999).
34. Muhammad, Z. et al. Excess 210Pb inventories and fluxes along the continental slope and basins of the Gulf of Papua. *J. Geophys. Res. Earth Surf.* **113** https://doi.org/10.1029/2006JF000676 (2008).
35. Courtois, A. et al. Short-term sediment dispersal via 234Th and 7Be sediment geochronology: The Mississippi River Delta Front. *Water* 16, (2024). https://doi.org/10.3390/w16030463
36. Baskaran, M. et al. Atmospheric fluxes of 7Be and 210Pb at Galveston and College Station, Texas. *J. Geophys. Res. Atmos.* **98**, 20555–20571. https://doi.org/10.1029/93JD02182 (1993).
37. Esri. Surface Volume (3D Analyst Tools). (2026).

38. Esri *TIN in ArcGIS Pro* (2026).
39. Goodbred, S. L. & Kuehl, A. Floodplain processes in the Bengal Basin and the storage of Ganges–Brahmaputra river sediment: an accretion study using 137Cs and 210Pb geochronology. *Sed Geol.* https://doi.org/10.1016/S0037-0738(98)00082-7 (1998).
40. Comans, R. N., Haller, M. & De Preter, P. Sorption of cesium on illite: non-equilibrium behaviour and reversibility. *Geochim. Cosmochim. Acta*. **55** (2), 433–440. https://doi.org/10.1016/0016-7037(91)90002-M (1991).
41. Cremers, A., Elsen, A., Preter, P. D. & Maes, A. Quantitative analysis of radiocaesium retention in soils. *Nature* **335** (6187), 247–249. https://doi.org/10.1038/335247a0 (1988).
42. Warner, J. C. et al. COAWST modeling system. *Ocean. Model.* **35**, 230–244. https://doi.org/10.1016/j.ocemod.2010.07.010 (2010).
43. Shchepetkin, A. F. & McWilliams, J. C. Correction and commentary for Ocean forecasting in terrain-following coordinates: Formulation and skill assessment of the regional ocean modeling system by Haidvogel et al., J. Comp. Phys. 227, pp. 3595–3624. *J. Comput. Phys.* 227, 3595–3624, (2009). https://doi.org/10.1016/j.jcp.2009.09.002
44. Booij, N. et al. Third-generation wave model. *J. Geophys. Res. Oceans*. **104**, 7649–7666. https://doi.org/10.1029/98JC02622 (1999).
45. Jacob, R. et al. M×N communication in CCSM3. *Int. J. High. Perform. Comput. Appl.* **19**, 293–307. https://doi.org/10.1177/1094342005056116 (2005).
46. Cummings, J. A. & Smedstad, O. M. Variational data assimilation. In *Data Assimilation for Atmospheric*. *Ocean. Hydrologic Appl.* **2**, 303–343. https://doi.org/10.1007/978-3-642-35088-7_13 (2013).
47. Helber, R. W. et al. Validation Test Report for the Improved Synthetic Ocean Profile (ISOP) System, Part I: Synthetic Profile Methods and Algorithm, *Naval Res. Lab. Oceanogr. Div. Stennis Space Cent. MS*, **125**, (2013).
48. Chapman, D. C. Numerical treatment of cross-shelf open boundaries in a barotropic coastal ocean model. *J. Phys. Oceanogr.* **15**, 1060–1075. https://doi.org/10.1175/1520-0485(1985)015%3C1060 (1985). :NTOCSO%3E2.0.CO;2.
49. Corbett, D. R. et al. An evaluation of mud dynamics in the Mississippi River deltaic region. *Mar. Geol.* **209**, 91–112. https://doi.org/10.1016/j.margeo.2004.05.028 (2004).
50. Saha, S. et al. NCEP Climate Forecast System Version 2 (CFSv2) [Dataset], (2011). https://doi.org/10.5065/D61C1TXF
51. Flather, R. A. A tidal model of the northwest European continental shelf. *Mem Soc. R Sci. Liege* (pp. 141–164 ), 10, 141–164, (1976).
52. Marchesiello, P., McWilliams, J. C. & Shchepetkin, A. Open boundary conditions for long-term integration of regional oceanic models. *Ocean. Model.* **3**, 1–20. https://doi.org/10.1016/S1463-5003(00)00013-5 (2001).

53. Ou, Y. & Xue, Z. G. Hydrodynamic and biochemical impacts on the development of hypoxia in the Louisiana–Texas shelf – Part 1: roles of nutrient limitation and plankton community, *Biogeosciences* 21, 2385–2424, (2024). https://doi.org/10.5194/bg-21-2385-2024
54. Warner, J. C. et al. A wetting and drying scheme for ROMS. *Comput. Geosci.* **58**, 54–61. https://doi.org/10.1016/j.cageo.2013.05.004 (2013).
55. Zang, Z. et al. A Two Decadal (1993–2012) Numerical Assessment of Sediment Dynamics in the Northern Gulf of Mexico. *Water* 11, 938, (2019). https://doi.org/10.3390/w11050938
56. Zang, Z. et al. Numerical study of sediment dynamics during hurricane Gustav. *Ocean. Model.* **126**, 29–42. https://doi.org/10.1016/j.ocemod.2018.04.002 (2018).
57. Warner, J. C. et al. Development of a three-dimensional, regional, coupled wave, current, and sediment-transport model. *Comput. Geosci.* **34**, 1284–1306. https://doi.org/10.1016/j.cageo.2008.02.012 (2008).
58. Sherwood, C. R. et al. Cohesive and mixed sediment in the Regional Ocean Modeling System (ROMS v3.6) implemented in the Coupled Ocean–Atmosphere–Wave–Sediment Transport Modeling System (COAWST r1234). *Geosci. Model. Dev.* **11**, 1849–1871. https://doi.org/10.5194/gmd-11-1849-2018 (2018).
59. Sha, X. et al. Characterization and modeling of sediment settling, consolidation, and suspension to optimize coastal Louisiana restoration. *Estuar. Coast Shelf Sci.* **203**, 137–147. https://doi.org/10.1016/j.ecss.2018.02.008 (2018).
60. Lo, E. L. et al. Experimental study of cohesive sediment consolidation and resuspension identifies approaches for coastal restoration: Lake Lery, Louisiana. *Geo-Mar. Lett.* **34**, 499–509. https://doi.org/10.1007/s00367-014-0381-3 (2014).
61. Soulsby, R. *Dynamics of Marine Sands*. (1997).
62. Renfro, A. A. et al. The sediment budget of an urban coastal lagoon (Jamaica Bay, NY) determined using 234Th and 210Pb. *Coast Shelf Sci.* **180**, 136–149. https://doi.org/10.1016/j.ecss.2016.06.008 (2016).
63. Denommee, K. C. et al. Hydrodynamic controls on muddy sedimentary-fabric development on the Southwest Louisiana subaqueous delta. *Mar. Geol.* **382**, 162–175. https://doi.org/10.1016/j.margeo.2016.09.013 (2016).
64. Allison, M. A. et al. Seasonal sediment storage on mudflats adjacent to the Amazon River. *Mar. Geol.* **125**, 303–328. https://doi.org/10.1016/0025-3227(95)00017-S (1995).
65. Twichell, D. et al. Subsurface control on seafloor erosional processes offshore of the Chandeleur Islands, Louisiana. *Geo-Mar. Lett.* **29**, 349–358. https://doi.org/10.1007/s00367-009-0150-x (2009).
66. Figueredo, N. et al. Sedimentary Processes and Instability on the Mississippi River Delta Front near the Shipwreck of the SS Virginia. *Water* **16**, 421. https://doi.org/10.3390/w16030421 (2024).
67. Duxbury, J. et al. Temporal Scales of Mass Wasting Sedimentation across the Mississippi River Delta Front Delineated by 210Pb/137Cs Geochronology. *J. Mar. Sci. Eng.* **12**, 1644. https://doi.org/10.3390/jmse12091644 (2024).

68. Dunn, F. E. et al. Projections of declining fluvial sediment delivery to major deltas worldwide in response to climate change and anthropogenic stress. *Environ. Res. Lett.* **14** https://doi.org/10.1088/1748-9326/ab304e (2019).
69. Tessler, Z. D. et al. A model of water and sediment balance as determinants of relative sea level rise in contemporary and future deltas. *Geomorphology* **305,** 209–220. https://doi.org/10.1016/j.geomorph.2017.09.040 (2018).
70. Syvitski, J. P. & Saito, Y. Morphodynamics of deltas under the influence of humans. *Glob Planet. Change*. **57**, 261–282. https://doi.org/10.1016/j.gloplacha.2006.12.001 (2007).

# Figures

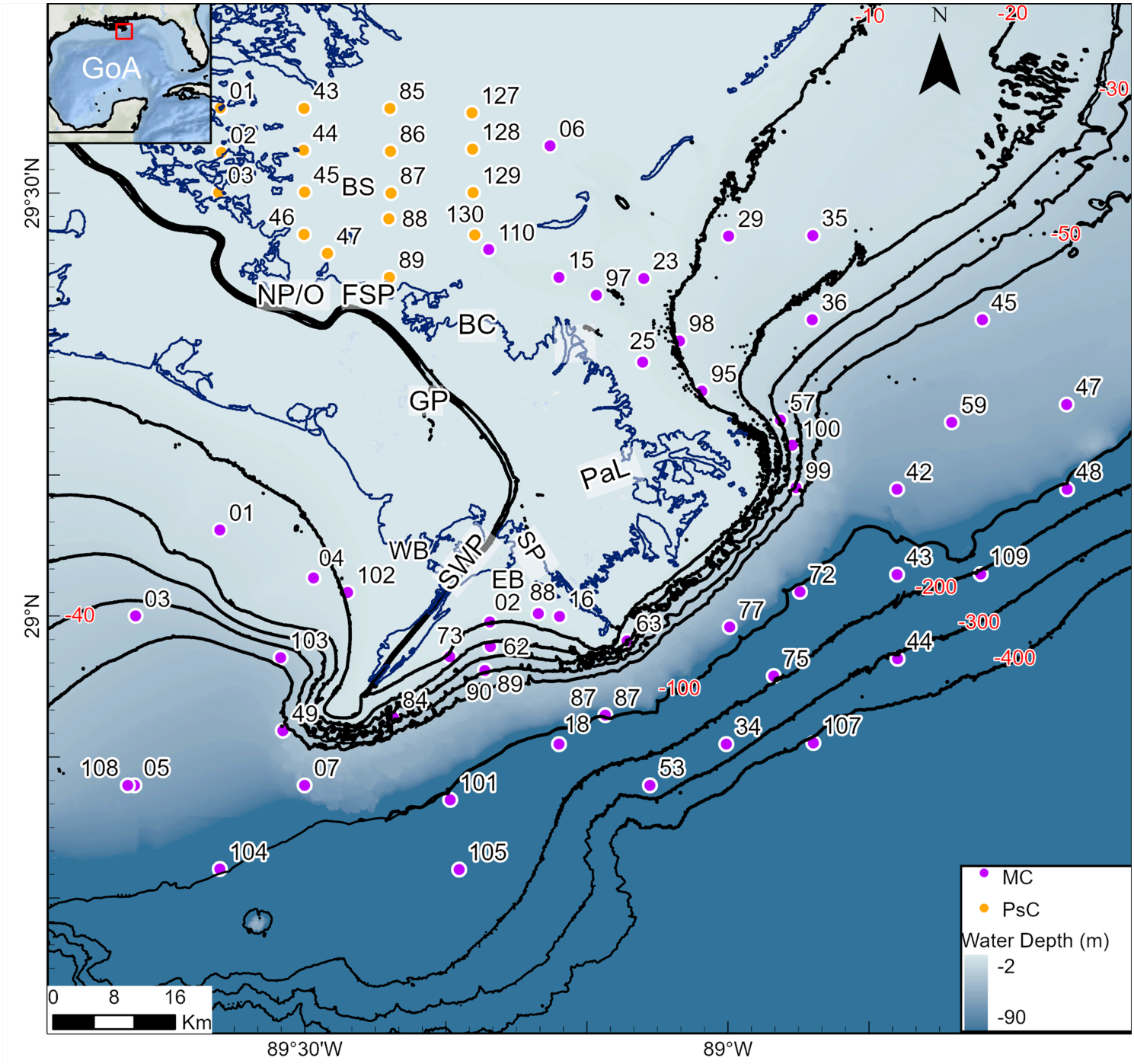



**Figure 1**

Bathymetric map [26] of offshore coring locations. Core locations symbolized in purple, multicores (MC), were collected using the MC800 onboard the *R/V Point Sur*. Core locations symbolized in orange are push cores (PsC) collected on a smaller 26-ft boat on a separate cruise. Black lines are bathymetric contours denoted by the red labels. (BS=Breton Sound, NP/O=Neptune Pass/Ostrica, FSP=Fort St. Phillip, BC=Baptiste Collette, MP=Main Pass, EB=East Bay, WB=West Bay, SWP=Southwest Pass, SP=South Pass, PaL=Pass a Loutre).

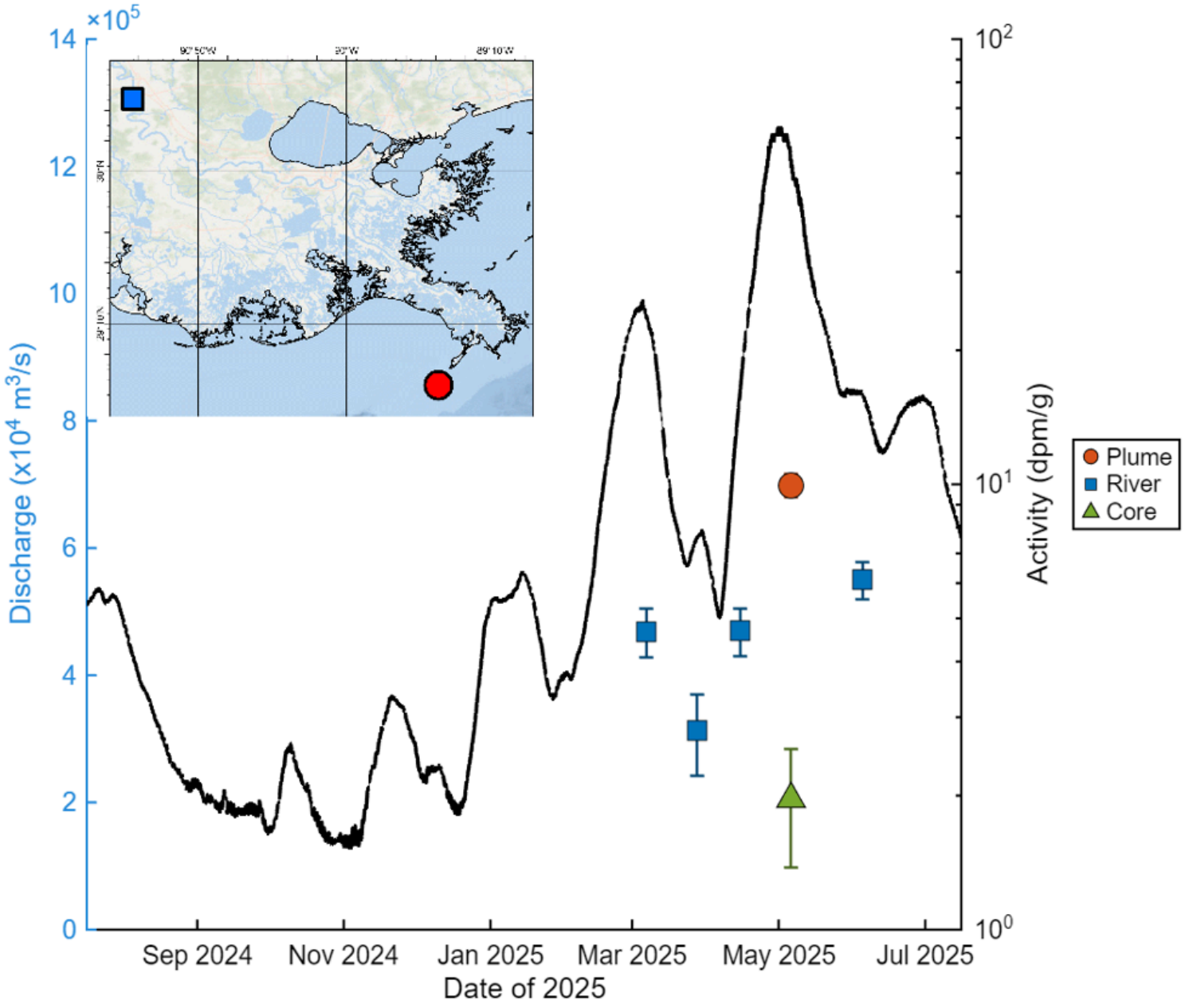



**Figure 2**

Hydrograph of river discharge for WY 2025 measured at station USGS-07374000 in Baton Rouge. Blue points are $^{7}$Be activity measured from the sediment sampled from the river channel near river-mile 228. The red point is the $^{7}$Be activity measured from the sediment sampled from the offshore river plume. The green point is the average $^{7}$Be activity of the 0-3 cm samples of the offshore sediment cores where $^{7}$Be was detectable. Inset map shows locations of river suspended sediment samples taken at river mile 228 (blue square) and an approximate location of where the plume ss sample (red circle) was collected offshore of the delta.

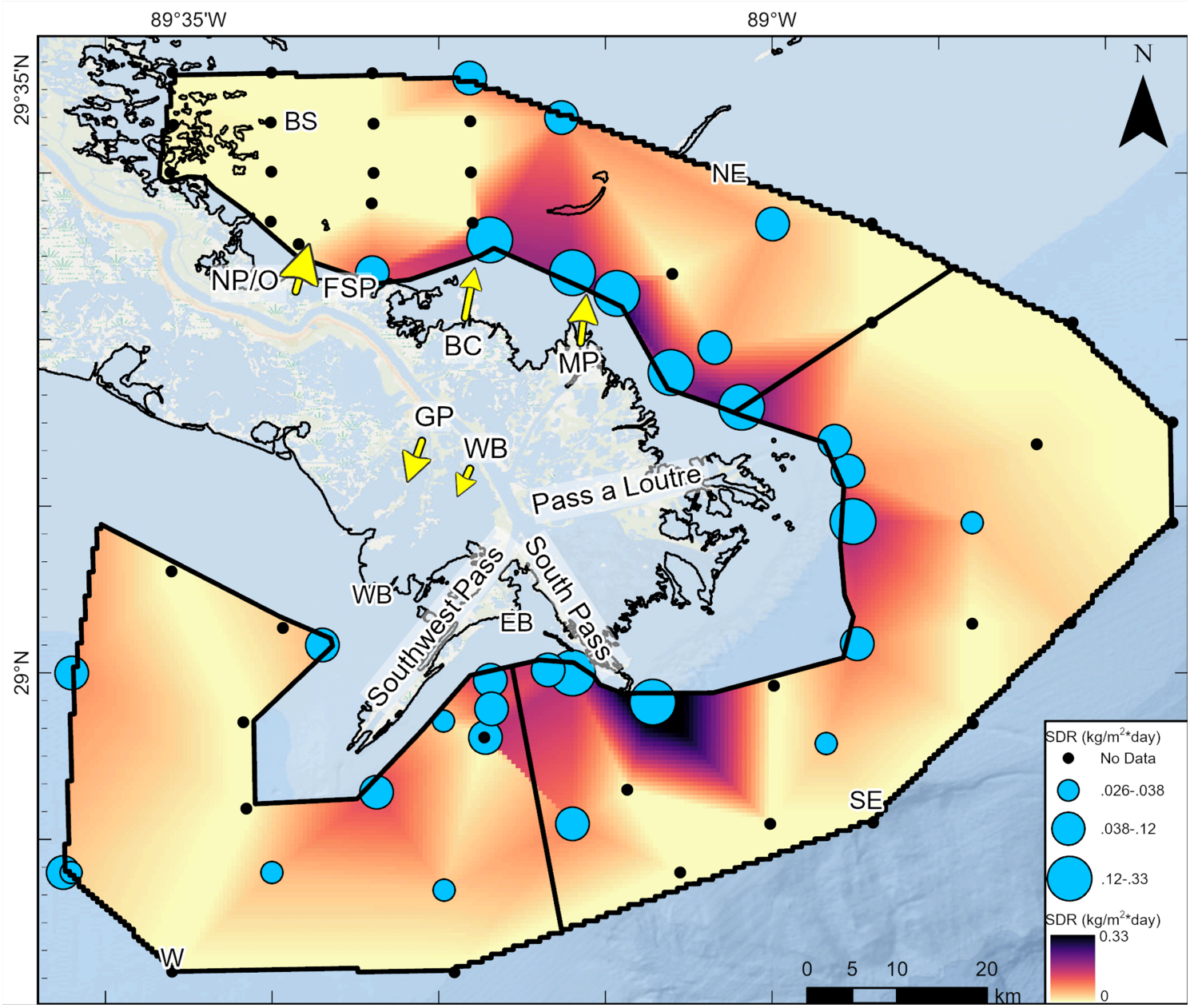
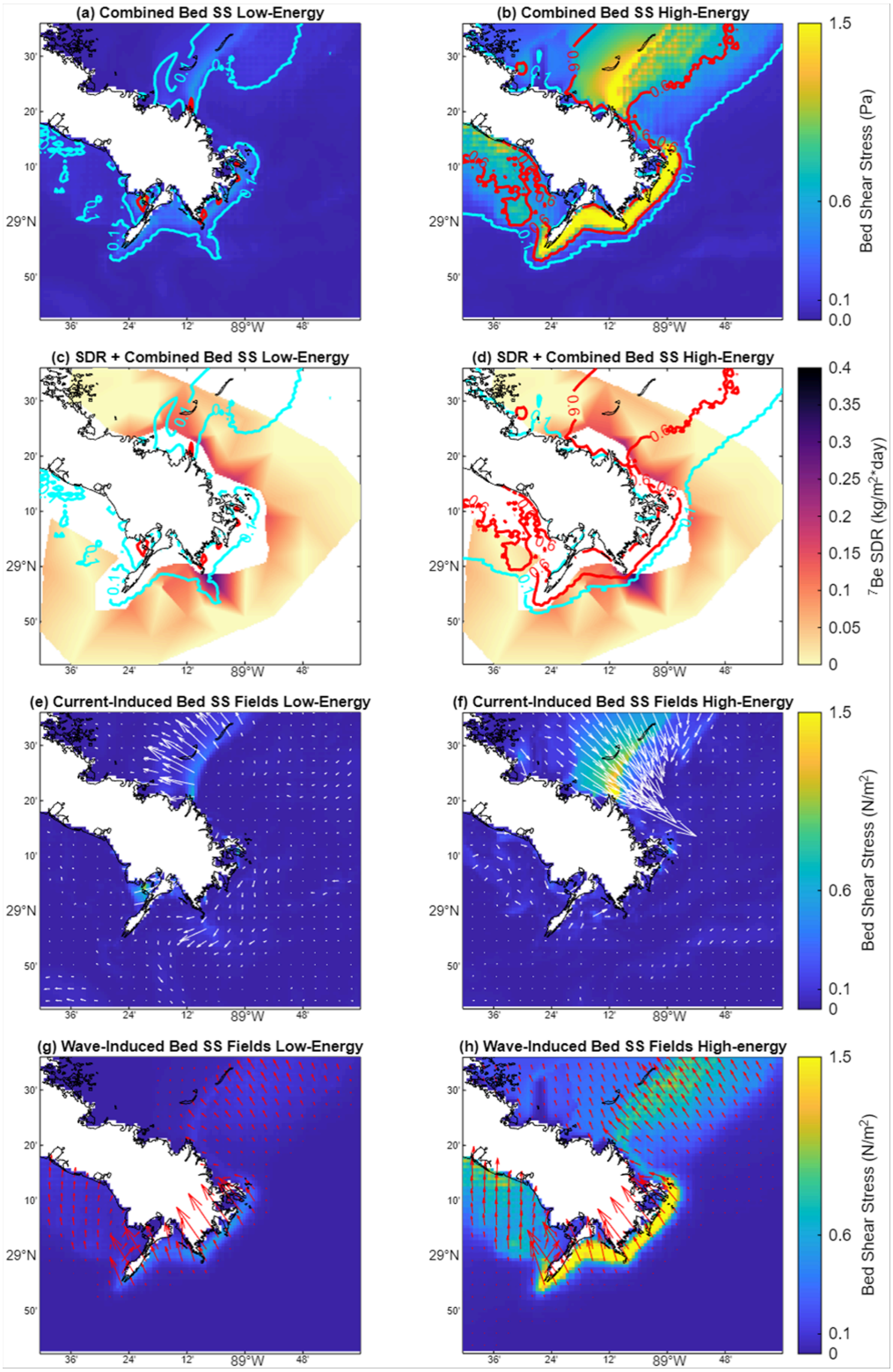



**Figure 3**

Map of core locations overlain onto the interpolated SDR surface. Core location points are proportional to SDR values. Yellow arrows indicate % of flow measured below Belle Chasse through each of the northern passes measured by Allison et al. 2022. (BS=Breton Sound, NP/O=Neptune Pass/Ostrica, FSP=Fort St. Phillip, BC=Baptiste Collette, MP=Main Pass, EB=East Bay, WB=West Bay, W=West, SE= Southeast, NE=Northeast)




## Figure 4

a. and b. Modelled combined wave and current bed shear stresses for high and low energy periods from which the 0.1 (teal) and 0.6 (magenta) Pa contours were extracted. Panels c. and d. are the interpolated SDR surface with the 0.1 Pa and 0.6 Pa combined bed shear stress contours overlain for both. Panels e. and f. are the current-induced bed shear stress surface and fields (arrows showing magnitude of modelled bed shear stress) for the two modelled periods. Panels g. and h. are the wave-induced bed

shear stress surface and fields (arrows showing magnitude of modelled bed shear stress) for the two modelled periods.
Figure modified from Zang et al. (2019).

## Supplementary Files

This is a list of supplementary files associated with this preprint. Click to download.

- MRDSedimentBudget2025SciRepSupplementaryWalton.docx
- MRD7BeActivity.csv
- MRDSurfaceGrainSize.csv